International Journal of Impact Engineering 195 (2025) 105128

Contents lists available at ScienceDirect

International Journal of Impact Engineering

journal homepage: www.elsevier.com/locate/ijimpeng

Strain rate sensitivity of rotating-square auxetic metamaterials

Behrad Koohbor [a,b,*], Kazi Zahir Uddin [a], Matthew Heras [a], George Youssef [c], Dennis Miller [d], Subramani Sockalingam [d], Michael A. Sutton [d], Thomas Kiel [e]

[a] *Department of Mechanical Engineering, Rowan University, 201 Mullica Hill Rd., Glassboro, NJ 08028, USA*
[b] *Advanced Materials and Manufacturing Institute, Rowan University, Glassboro, NJ 08028, USA*
[c] *Experimental Mechanics Laboratory, Department of Mechanical Engineering, San Diego State University, 5500 Campanile Drive, San Diego, CA 92182, USA*
[d] *Department of Mechanical Engineering, University of South Carolina, 300 Main St., Columbia, SC 29208, USA*
[e] *U.S. Army DEVCOM Armaments Center, Picatinny Arsenal, NJ, USA*

ARTICLE INFO

Keywords:
Auxetic
Additive manufacturing
Multiscale mechanics
Poisson's ratio
Mechanical metamaterials
Strain rate

ABSTRACT

This study provides an in-depth analysis of the mechanical behavior of rotating-square auxetic structures under various strain rates. The structures are fabricated using stereolithography additive manufacturing with a flexible resin. Mechanical tests performed on structures include quasi-static, intermediate, and high strain rate compression tests, supplemented by high-speed optical imaging and two-dimensional digital image correlation analyses. In quasi-static conditions (5×10^{-3} s^{-1}), multiscale measurements reveal the correlation between local and global strains. It is shown that cell hinges play a significant role in structural deformation and load-bearing capacity. In drop tower impact conditions (intermediate strain rate of *ca.* 200 s^{-1}), the auxetic structures display significant strain rate hardening compared to loading at quasi-static rates. The thin-hinge structures maintain a Poisson's ratio of approximately -0.8, showing higher auxeticity than slow-rate compression tests. High strain rate conditions (*ca.* 2000s^{-1}) activate additional deformation mechanisms, including a delayed state of equilibrium exemplified by a heterogeneous distribution of lateral strains, possibly due to stress wave interactions and inertial stresses. The study further reveals nonlinear correlations between Poisson's ratio, strain, and strain rate, indicating reduced auxeticity at higher strain rates. These observations are discussed in terms of complex wave interactions and the strain rate hardening characteristics of the base polymer.

1. Introduction

Distinguished by their unique mechanics, mechanical metamaterials have emerged as a class of advanced structures [1]. Distinct characteristics of these materials include tunable mechanical behavior such as a high stiffness-to-weight ratio, programmable Poisson's ratio, and enhanced energy absorption capabilities [2,3]. These characteristics are closely tied to the structural and geometric features of the structure, including cell connectivity and architectural configurations [4,5]. Precise tuning of these attributes enables specific nonlinear mechanical behavior for various strain rates [6]. The targeted nonlinear mechanics could be pivotal in designing flexible structures, including wearable electronics, smart materials, medical equipment, and self-recoverable materials in tissue engineering [7,8]. In these structures, the local morphology, rather than chemical composition, is key to their extraordinary mechanical properties [1,9,10]. For instance, nonlinear behavior in the form of larger internal cellular rotations can be initiated by introducing architected slender elements [9]. Such instabilities enable physics-driven functionalities like auxeticity and programmable shape morphing with superior energy absorption capacity [11,12]. As part of the broader concept of metamaterials, auxetic structures are known for their counterintuitive mechanical behavior, mainly driven by their negative Poisson's ratio, so that auxetic structures contract (expand) laterally under uniaxial compression (tension) [13,14]. Concurrently, auxetic structures exhibit superior strength, shear resistance, fracture toughness, and energy absorption under various loading conditions [15,16]. These unique characteristics position auxetic metamaterials as promising candidates for diverse applications such as biomedical devices, protective gear, vibration dampers, smart sensors, and flexible electronics [17-19]. Their potential extends into smart textiles, advanced filtration systems, phononic performance, and energy-efficient building materials.

Early analytical and experimental studies on auxetic metamaterials focused on the potential to obtain negative Poisson's ratios in foams,

---

[*] Corresponding author.
E-mail address: koohbor@rowan.edu (B. Koohbor).

https://doi.org/10.1016/j.ijimpeng.2024.105128
Received 24 March 2024; Received in revised form 5 August 2024; Accepted 16 September 2024

evolving into a rich array of geometries and applications that includes hierarchical laminates, polymeric and metallic lattices, and microporous polymers [20-22]. Auxetic foams were produced by transforming conventional open-cell structures into re-entrant voids using hot compression [23]. Further research has broadened the scope of auxetic foams and their fabrication techniques, such as biaxial or triaxial hot compression, for materials such as polyurethane, epoxy resins, and metallic foams [24,25].

The enclosed exploration extends these concepts to periodically arranged unit cell-based structures, where the specific geometrical configurations determine their auxetic nature. Innovative geometries such as reentrant hexagonal honeycombs, chiral structures, rotating-rigid units, perforation-based structures, and Origami- and Kirigami-based metamaterials have been well-established [26-32]. While these auxetic geometries contribute to distinct structural design and deformation mechanisms, they often face limited isotropy, suboptimal mechanical stability under different loading conditions, and precise fabrication complexity [33,34].

As an emerging class of mechanical metamaterials, rotating-square cell auxetics stand out for their ability to achieve high degrees of isotropy and pronounced auxetic behavior, with their isotropic auxeticity correlated to the distinctive, hinge-based rotating mechanism in each square unit. In early studies, Grima et al. introduced different geometries (*e.g.,* triangle, square, parallelogram, and rectangle) as rotating rigid units [35-37]. The fabrication of these auxetics can be attained by placing periodically or randomly oriented slits with the ability to extend the geometry from 2D planar sheets to 3D cuboidal-shaped networks. Early observations indicated that the degree of Poisson's ratio modulation can be altered for rectangle unit cells, while square unit cells always exhibited negative Poisson behaviors [37]. In recent studies, hierarchical unit cells have also been introduced in rotating rigid unit mechanisms [38,39]. It has been demonstrated that desired degrees of auxeticity can be tuned in such hierarchical structures by controlling the size and distribution of pores and slits. While there is an ongoing effort to achieve complex geometries for rotating-unit auxetics, researchers have proposed different analytical models to predict the mechanical properties of these metamaterials [40,41]. The modeling efforts typically characterize the deformation of individual unit cells and extrapolate this behavior to the entire structure. Common assumptions in these models include perfectly rigid, freely rotating cells. However, these assumptions may fall short in structures featuring soft materials, thick hinge geometric configurations, or those subjected to high strain rate loading conditions, noting that the latter can activate strain rate hardening of the cell hinges, thereby hindering the resistance-free rotation of the solid cells [42,43].

Multiscale mechanical characterizations under quasi-static and dynamic loading conditions are necessary to capture the complex kinematics of rotating-square auxetic structures. In quasi-static loading, the rotational degree of freedom of solid cells can induce higher compressibility and enhance energy absorption capacities without compromising the structural strength [37,44,45]. The rotation of unit cells plays a significant role in controlling the synergy between auxeticity, load-bearing, and overall energy absorption under quasi-static loading rates [6,16,46]. However, earlier studies found discrepancies in the crushing nature and deformation mode of different auxetic geometry for variable strain rate conditions, reporting different peak stresses [47,48].

A distinct knowledge gap exists in the nonlinear deformation/rotation nature of rotating square auxetics in various strain rate conditions. This gap is notable in scenarios involving high-speed impacts to uncover the governing deformation mechanism. Therefore, understanding the fundamental mechanics of rotating square auxetic networks and their base material for a wide range of strain rate conditions is imperative, noting that previous studies reported specific rate-dependent characteristics in the mechanical response of parent material and its derivatives [49,50]. In addition, the domain of small-scale auxetics is relatively less explored. It is unclear if the auxetic nature and energy absorption properties observed in larger prototypes will seamlessly transition to down-scaled counterparts. An in-depth investigation of deformation response at multiple strain rate conditions coupled with miniature scale rotating square auxetic fabrication can lead to the innovation of novel microscale apparatus, including shock absorbers in micro-electromechanical systems, micro-robotics, aerospace components, micro-implants, and impact-resistant microdevices, to name a few.

To address the abovementioned points, we investigate the mechanical properties and strain rate sensitivity of rotating-square auxetic structures with millimetric and sub-millimetric architectural features fabricated by stereolithography additive manufacturing. The robust experimental setup reported herein includes quasi-static, intermediate strain rate (drop tower impact), and high strain rate (Split Hopkinson Pressure Bar) tests to explore the rate-dependent mechanical responses across a spectrum of strain rates. We employ digital image correlation (DIC) in conjunction with high-speed optical imaging systems to characterize the kinematic fields and investigate the strain rate sensitivity of the structures and their relationships with the base polymer characteristics. To the best of the authors' knowledge, the present study is the first to connect the dots between the auxeticity, load-bearing capacity, and the loading rate effects in rotating-square auxetic structures.

2. Experiments

2.1. Material and sample fabrication

Rotating-square auxetic structures with two different hinge thicknesses of 200 and 400 μm (hereafter referred to as *thin-hinge* and *thick-hinge* structures) were fabricated by stereolithography (SLA) additive manufacturing. The base material was a flexible 80A photopolymer resin (version V1.1, Formlabs, MA, USA). Some of the favorable characteristics of this material include rubber-like behavior with a stiffness comparable to thermoplastic polyurethane (TPU), as well as resistance to repeated bending and compression loadings. Samples with dimensions illustrated in Fig. 1 were printed and then subjected to a post-printing curing cycle according to the resin manufacturer's recommended guidelines. All samples in this work were 3D printed with a layer thickness of 50 μm. Before curing, the as-printed samples were washed in two cycles in isopropyl alcohol (IPA) solvent, using fresh solvent for the second wash to remove waxiness. Next, the samples were subjected to a thermal curing process at 60 °C for 10 min. This process ensured that parts reached their optimal mechanical properties as recommended by the resin manufacturer.

After curing, the front surface of the samples was coated with a thin layer of matte white paint to cover their natural semi-translucency. A random pattern of black speckles was then sprayed onto the white substrate. The resultant pattern (Fig. 1d) was suitable for image correlation in quasi-static loading conditions, discussed in Section 3.2. The nominal densities of the thin and thick-hinge structures examined in this work were 533 and 601 kg/m^3, respectively.

In addition to the rotating square structures described above, sub-sized dogbone and cube samples were fabricated and used to characterize the mechanical response and strain rate sensitivity of the base polymer (*i.e.*, flexible 80A photopolymer). The **Supplementary Information** document (**Sec. S1)** includes details regarding the dimensions and mechanical testing of the base material in tension. The 3D printing process of the tensile and compression test samples followed the steps to manufacture the rotating-square structures.

2.2. Quasi-static testing (Slow strain rate)

Slow strain rate tests were performed to characterize (1) the mechanical and strain rate sensitivity of the base photocurable polymer and (2) the load-bearing behavior of the thin and thick-hinge structures

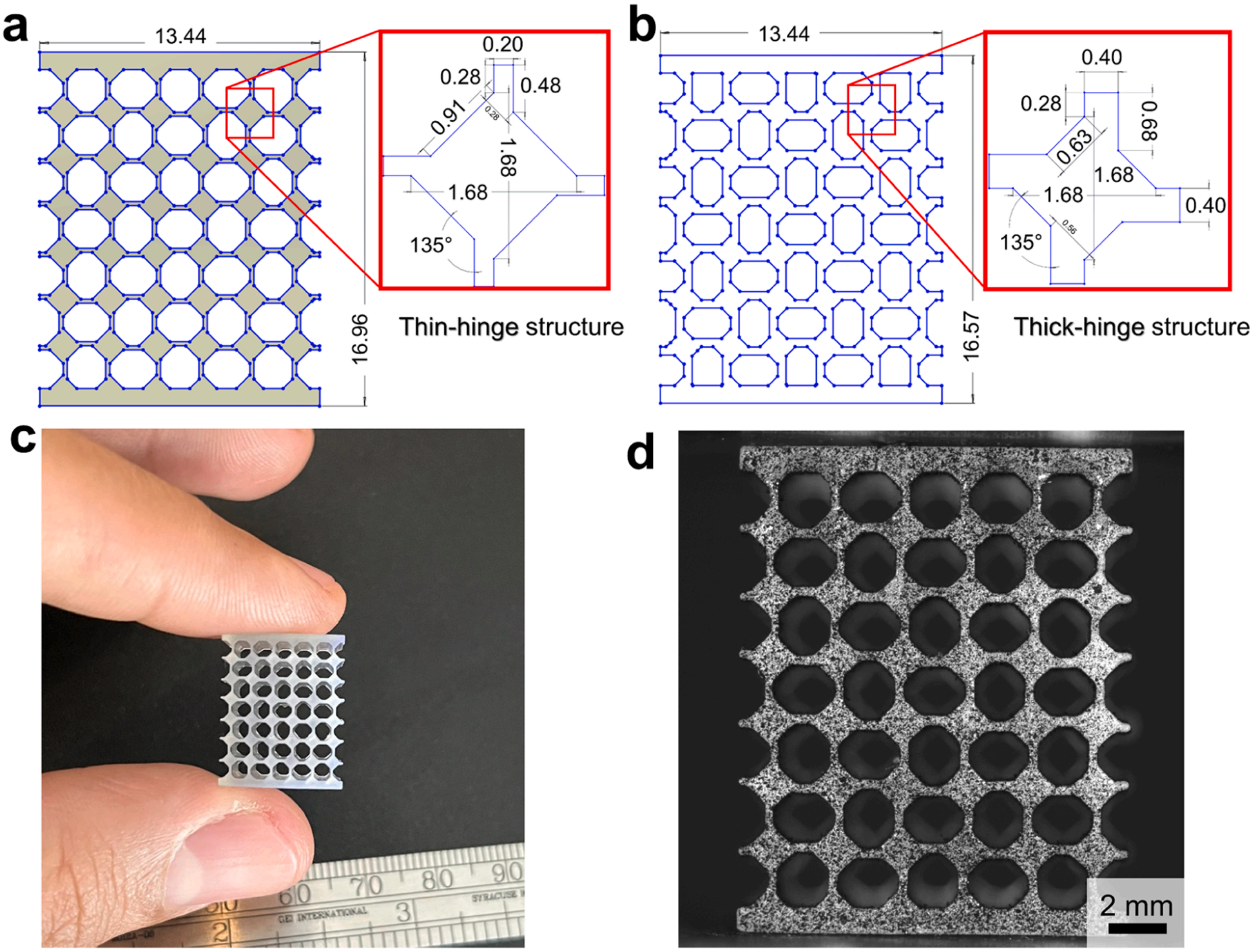

Fig. 1. Novel rotating square metamaterials geometry and dimensions (in mm) of (a) thin- and (b) thick-hinge structures with a depth of 11.2 mm. Pictorial views of post-cured thin-hinge structure (c) before and (d) after applying the speckles.

under quasi-static compressive conditions. Tensile tests were performed at crosshead speeds of 0.1 and 100 mm/min on nonstandard double-reduced dog-bone samples designed with gauge length, gauge width, and thickness of 4 × 1 × 1 mm (see **Supplementary Information** document for additional details). The three orders of magnitude of difference in crosshead speed were chosen intentionally to enable characterizing the strain rate-dependent mechanical response of the base polymer. Similarly, quasi-static compression tests were performed on 12 × 12 × 12 mm cubes at the same two crosshead speeds of 0.1 and 100 mm/min. All quasi-static tests were conducted using a Shimadzu AGS-X electromechanical load frame with a 10 kN load cell and ±1 N load sensitivity.

The engineering tensile and compressive stress-strain responses of the samples were determined in triplicates to ensure repeatability. Engineering strain was measured in the gauge section using the “optical extensometer” option in the image correlation software Vic-2D (Correlated Solutions, Inc., SC, USA). The average stress-strain response was used to assess strain rate sensitivity and measure Poisson’s ratio for the base polymer. The results indicate that the base material exhibits rate-independent Poisson’s ratio values of *ca.* 0.45.

Quasi-static compression tests with a crosshead speed of 5 mm/min (equivalent to a nominal strain rate of 5×10^{-3} s^{-1}) were also performed on thin and thick-hinge rotating-square structures. The engineering (nominal) stress-strain curves of the structures were obtained following the approach reported previously by Deng et al. [6] and Uddin *et al.* [51]. The nominal stress was determined by dividing the force by the projected cross-sectional area of each structure, *i.e.*, a 13.4 × 11.2 mm^2 (see Fig. 1).

2.3. *Drop tower impact testing (Intermediate strain rate)*

Controlled impact loading (hereafter referred to as intermediate strain rate) was applied on solid cube samples and rotating square structures. A custom-designed drop tower impact instrument was used to release a free-falling mass of 900 g from a height of 650 mm. The kinetic energy of the drop weight was sufficient to deform the rotating-square structures beyond their apparent densification strain, as discussed in more detail in a forthcoming section. Conversely, energy transfer to the solid cubes only compressed the sample by ~20%. Impact loads applied on samples were recorded by a load cell (ICP Force Sensor, 208C03, Piezotronics, NY, USA). The deformation field was analyzed by 2D DIC using images captured at a frame rate of 14,500 fps (see **Supplementary Information** document for more details). The nominal strain rates applied on samples during impact tests were determined as the slope of a linear fit to the strain-time data in each case. Accordingly, nominal strain rates of 65 s^{-1} and ~200 s^{-1} were determined for the solid cube samples and rotating-square structures, respectively. The **Supplementary Information** document includes a pictorial view of the drop tower impact instrument used in this research.

Considering the relatively low spatial resolution of the images acquired by the high-speed camera during drop impact tests (11.6 pixel/mm at 14,500 fps, also see **Figure S3** and **Table S1** in the **Supplementary Information** document), only the macroscopic deformations were measured by 2D-DIC, with the structural voids on the surface of the sample providing sufficient contrast for image correlation analyses. Consequently, DIC subsets (correlation windows) with dimensions close to the void sizes had to be used. The macroscale deformation of the structures measured by DIC allowed the determination of axial and transverse global strains during the impact event, resolving the apparent Poisson's ratios.

2.4. Split hopkinson pressure bar (High strain rate) tests

High strain rate compression experiments were conducted on thin and thick-hinge rotating-squares structures with a split Hopkinson pressure bar (SHPB) apparatus. The polycarbonate incident and transmitter bars in the utilized SHPB apparatus had a diameter of 25.4 mm and a length of 1830 mm. The sample was placed between the two bars with a thin layer of lithium grease that also served as lubricant. The strain signals generated in the bars were collected using strain gauges placed in the middle of each bar. The strain signals were used with well-established SHPB equations to report the strain rate and stress in the deformed structures. The temporal variations of strain rate ($\dot{\varepsilon}_s$) and stress (σ_s) in the structures were determined by

$$\dot{\varepsilon}_s(t) = -\frac{2C_b}{l_s}\varepsilon_r(t) \tag{1}$$

$$\sigma_s(t) = \frac{E_b A_b}{A_s}\varepsilon_r(t) \tag{2}$$

where, l_s, A_s, and A_b denote sample length, sample cross-sectional area, and the bar cross-sectional area, respectively. C_b and E_b are the sound velocity and elastic modulus of the bar material, respectively, and ε_r is the time-resolved strain of the reflected pulse collected by the strain gauge in the incident bar. More information about the utilized SHPB apparatus and data analysis methods can be found in Ravindran *et al.* [52,53]. Further details regarding the stress equilibrium state during SHPB tests are discussed in the forthcoming sections. Photograph of the SHPB instrument is shown in the **Supplementary Information** document.

Strain fields developed in the structures were measured by 2D-DIC using 128 images acquired with a Hypervision HPV-X2 (Shimadzu) ultrahigh-speed camera at 500,000 fps and image resolution of 400 × 250 pixels. The camera was fitted with a 100 mm macro lens. A high-intensity flash unit was used for lighting. Similar to drop tower impact tests described in Section 2.3, the low spatial resolution of the Shimadzu camera made it difficult to measure local strains in different parts of the impacted structure, limiting the 2D-DIC high strain rate deformation analyses to macroscale deformation characterization of the structures. Nevertheless, the strain data collected from full-field measurements were sufficient to determine the global strains and strain rate-dependent Poisson's ratio in our high strain rate testing.

Global strain in an SHPB-tested sample can be readily determined by integrating Eq. (1) with respect to time. While the time integration was performed to cross-verify the strain measurements by the two approaches (*i.e.*, DIC and SHPB equations), discussions regarding measured sample deformation, strain, and strain rates only include those obtained from image correlation.

2.5. Strain rate sensitivity characterization

The broad range of strain rates in this study, expanding beyond five orders of magnitudes, from 5×10^{-3} to $\sim 2000\text{s}^{-1}$, allows for quantitative characterization of the strain rate-dependent behavior of the structures. To quantify strain rate sensitivity and enable comparisons between the rate-dependent behavior of the structures and their constituent polymer, the strain rate sensitivity exponent, m_σ, was determined based on the following equation,

$$\sigma_h = \sigma_l(\dot{\varepsilon}_h/\dot{\varepsilon}_l)^{m_\sigma} \tag{3}$$

where, subscripts l and h represent the low and high strain rate conditions, respectively. The rate sensitivity exponent was determined from the slope of log-*log* curves correlating the ratios between the stresses and strain rates at high and low rates.

3. Results and discussions

3.1. Strain rate sensitivity of base polymer

The strain rate sensitivity of the base photocurable polymer was characterized based on the tensile and compressive testing. Fig. 2a presents the tensile and compressive stress-strain curves of the bulk samples at various strain rates. The compressive stress-strain responses are reported as positive quantities to improve visualization. The results in Fig. 2a indicate that the base material exhibits strong rate dependence in the broad range of tested strain rates. The rate-dependent compressive stresses for strain rates ranging between 1.3×10^{-4} s^{-1} and 65 s^{-1} are illustrated in Fig. 2b for three different compressive strain values (denoted in the legend of Fig. 2b). The extracted data points in the log-*log* graph in Fig. 2b are fitted with regression lines, the slopes of which indicate the rate sensitivity exponent of the base material, m_σ. The average m_σ for the base polymer was determined as 0.071 ± 0.006 for the range of experimental strain rates considered herein. Similar values for strain rate sensitivities were determined for tensile conditions as well. However, due to the limited range of strain rates used in tensile tests, we only show and utilize the compressive deformation results and the strain rate sensitivity data extracted from them. In later sections, the measured strain rate sensitivity exponent is used to interpret the rate-dependent mechanical behavior of the rotating-square structures.

3.2. Correlation between local and global strains in rotating square structure in low strain rate experiments

A multiscale deformation analysis is essential since the global mechanical deformation of the rotating-square structures is governed by several interdependent mechanisms activated at different strains. For example, the nearly resistance-free rotation of the solid squares at global engineering strains below 0.2 is facilitated by the bending of connecting hinges, as discussed in [51]. This strain range corresponds to a stress plateau, wherein the structure absorbs large amounts of strain energy [15]. Upon the saturation of the cell rotation, the solid squares contact one another, causing a rapid increase of strain hardening and densification of the structure. For a strain rate of 5×10^{-3} s^{-1}, the sequential deformation patterns are illustrated in Fig. 3 as equivalent (von Mises) strain contours for the thin- and thick-hinge structures at different global strains. Deformation fields in the structures are exemplified by the rotation of solid squares, leading to an inward lateral contraction (*i.e.*, negative Poisson effect) at smaller global strains. The densification stage initiates at strains >0.20, rapidly increasing local strains in the solid squares.

With the full-field strain measurements obtained at low strain rate conditions, it is possible to extract the local strain fields at specific locations. For example, local strain analyses are shown in Fig. 4, where the local equivalent strains are extracted from the 'squares' and 'hinges' and plotted as a function of the global strain. The results in Fig. 4 highlight the multiscale strain correlations based on the contribution of each structural feature (*i.e.*, solid square and cell hinge) to the global deformation of the structures. As shown in Fig. 4, the hinge strain in thin and thick-hinge structures follows the global strain evolution in trend and quantity.

In contrast, the variation of local strains on solid squares is exemplified by a modest initial increase, followed by an extended plateau up to *ca.* 0.4 global strains, eventually rising at a higher pace at strains >

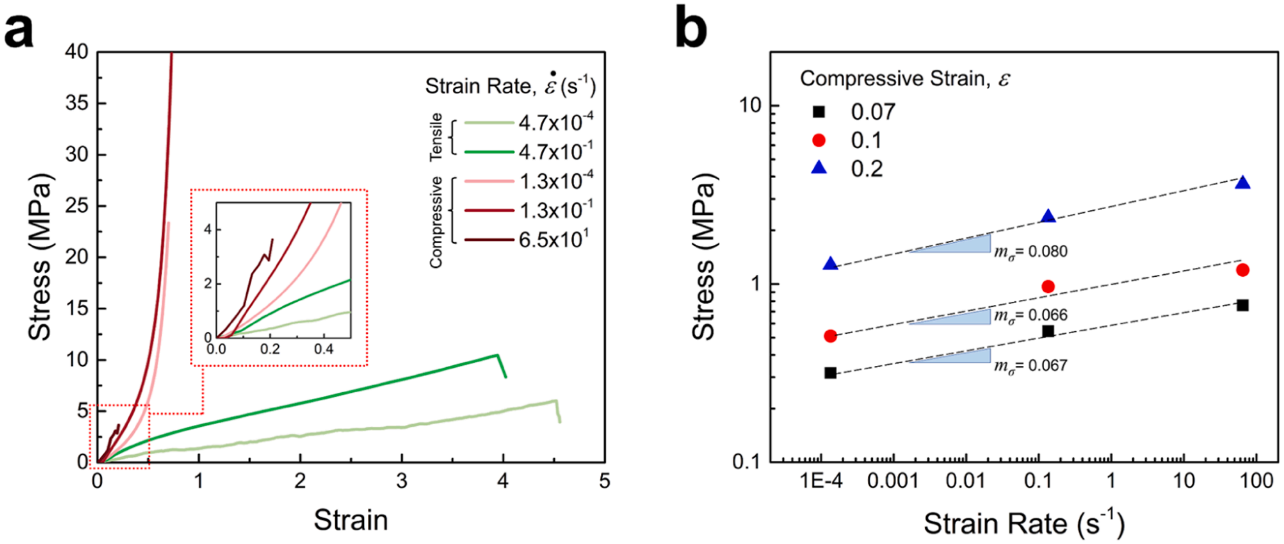

Fig. 2. (a) Tensile and compressive (plotted in the first quadrant for visualization) stress-strain curves for the base polymer at various strain rates. (b) Stress *vs*. strain rate at three different compressive strains with slopes representing the strain rate sensitivity exponents.

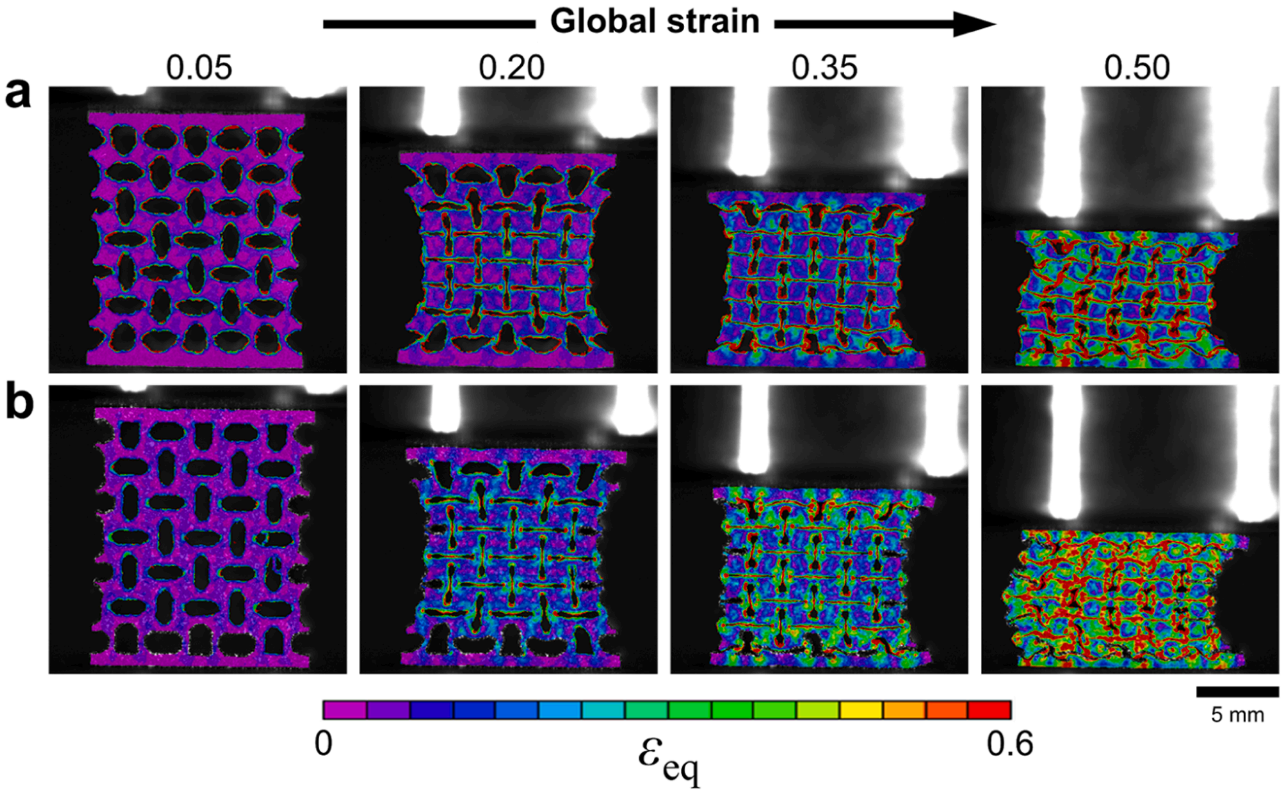

Fig. 3. Contour maps showing equivalent (von Mises) strain fields in (a) thin-hinge and (b) thick-hinge structures at different global strains at 5×10^{-3} s^{-1}.

0.4. A noteworthy observation is that the evolution of strains on hinges is independent of the cell hinge thickness. The local strain values developed on hinges increase monotonically with global strain in both structures, except for a clear knee point at approximately 0.2 global strain. While the anomaly in strain increase at 0.2 global strain was previously shown as a consequence of the saturation of rotational degrees of freedom in solid square units [51], the nearly one-to-one match between the global strain and local strains at hinges highlights the more pronounced contribution of the cell hinges to the macroscale deformation and load bearing capacity of the structures.

3.3. *Deformation and poisson's ratio in slow strain rates*

The global deformation response under quasi-static loading conditions was further analyzed to exploit the mechanics of the rotating-squares structure. First, the deformation behavior and strain fields were characterized by monitoring the row-wise lateral strains across the six rows in the structure (see Fig. 5a). Fig. 5b and Fig. 5c show the 2D-DIC measured lateral engineering strains (*i.e.*, transverse contraction normalized by the initial width) plotted as a function of global axial strains. The upper and lowermost cell rows behave differently than the

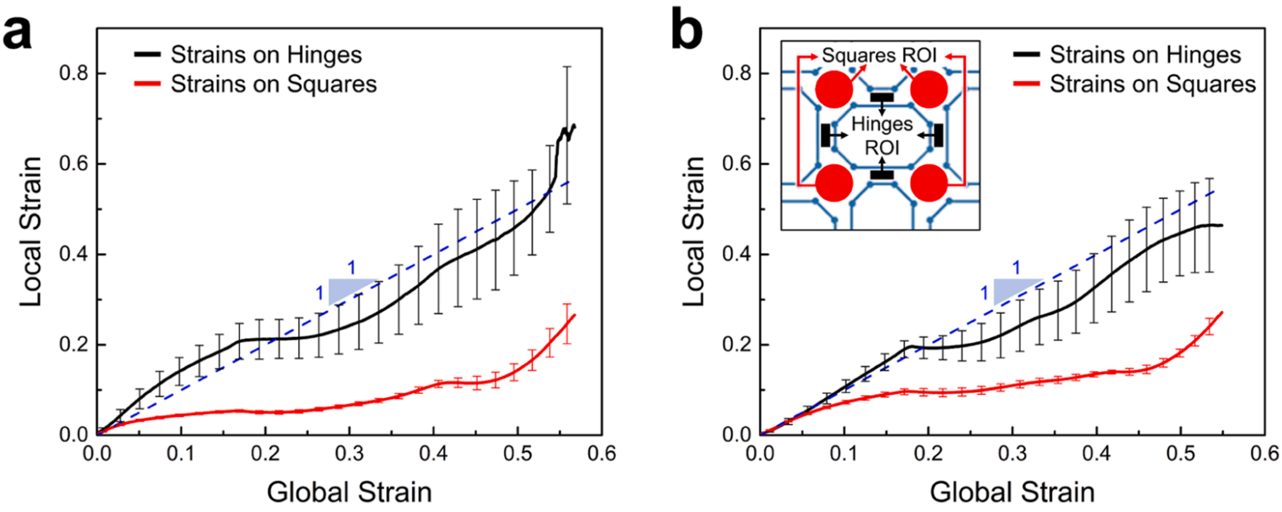

Fig. 4. Correlations between local (resolved from four regions of interest, ROI, at the center) and global strains in (a) thin-hinge and (b) thick-hinge rotating-square structures at low strain rate (5×10^{-3} s^{-1}). Scatter bars indicate the local variations, while the dashed straight lines are plotted to compare local and global strain values.

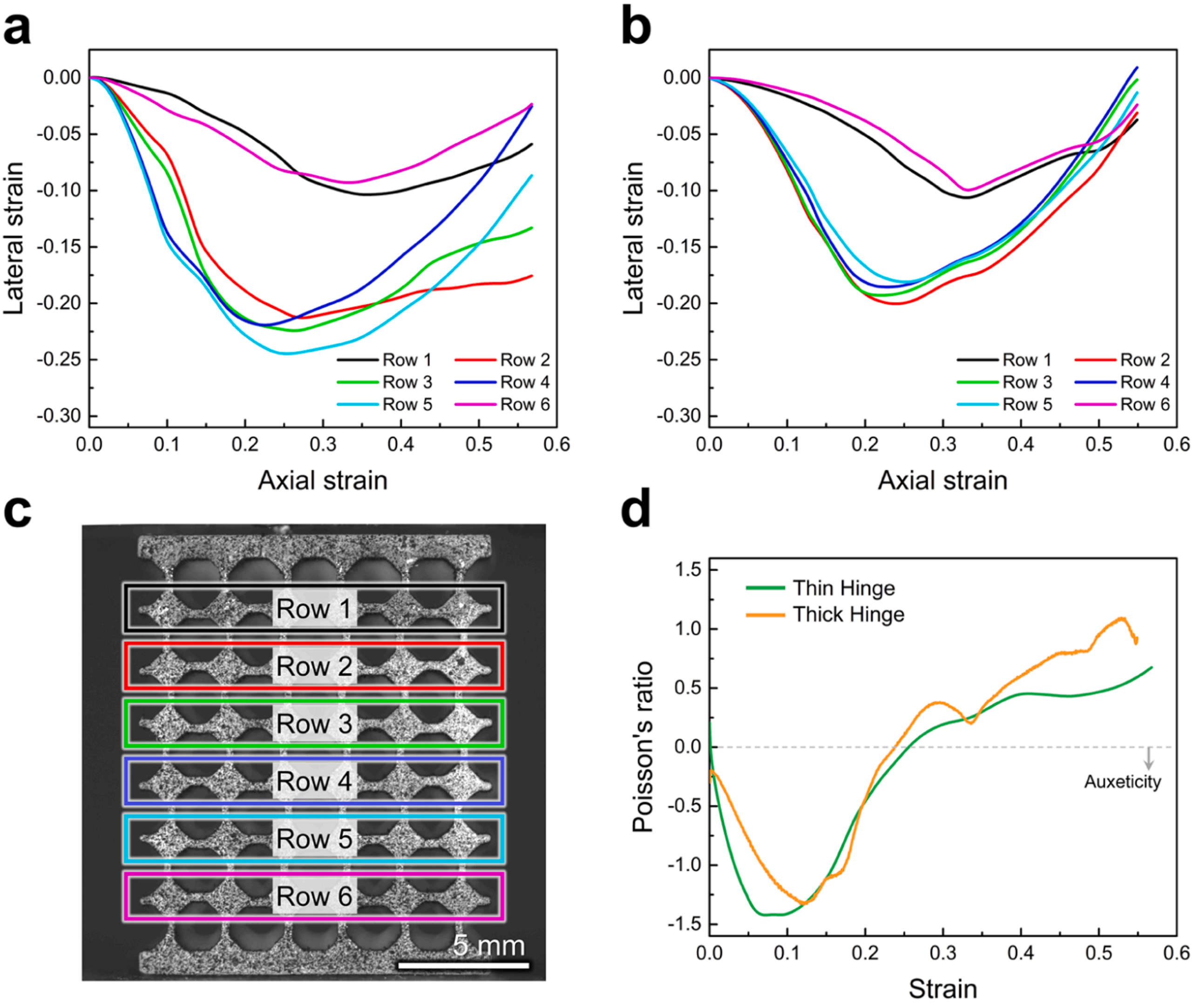

Fig. 5. Lateral strains with axial strain (shown in positive values) for (a) thin and (b) thick-hinge structures as a function of rows of unit cells (c), and (d) respective of Poisson's ratio at slow strain rate (5×10^{-3} s^{-1}).

middle four rows, primarily due to the boundary conditions. In other words, rows 1 and 6 exhibit smaller contractions (smaller negative lateral strains) than rows 2–5. Regardless of lateral strain magnitudes, all rows show inward contractions under axial compression, a deformation pattern confirming the auxetic behavior of our samples at macroscopic levels.

The lateral strain values measured for the four middle rows differ slightly between the thin and the thick structures, with the latter showing smaller lateral strains and implying a lower auxetic response. To quantify the degree of auxeticity, the evolution of macroscale Poisson's ratio with axial strain was determined for each structure. The apparent Poisson's ratios in this work were evaluated using the definition $\upsilon = -d\varepsilon_t/d\varepsilon_a$, wherein ε_t and ε_a denote average lateral (transverse) and axial strain components, respectively. The average lateral strain in all cases refers to the arithmetic average of the four lateral strains corresponding to the middle four cell rows. Apparent Poisson's ratios measured for the structures under slow strain rates (5×10^{-3} s^{-1}) are shown in Fig. 5d, indicating highly negative values at small strains, representing the auxetic nature of the samples. As anticipated from the local strain response discussed earlier, the thick-hinge structures show higher (less negative) Poisson's ratios, exemplifying lower auxeticity. Irrespective of their magnitudes, the Poisson's ratios for the structures follow similar trends, reverting their decreasing trend at axial strains between 0.1 and 0.15. The increasing trend leads to positive Poisson's ratios at axial strains of approximately 0.25, corresponding with the saturation of the rotational degree of freedom of the cells, elucidated earlier in Fig. 3 and discussed in detail in a recent report [51]. Poisson's ratios measured for the rotating-square structures here are consistent with those reported in earlier studies [15]. Theoretical studies of similar rotating-square structures suggest a constant Poisson's ratio equal to -1 irrespective of the applied strain, due to the resistance-free rotation of the cells [27]. However, previous finite element simulations [45] and experimental measurements [15,54] suggest that these structures experience the highest degree of auxeticity (*i.e.*, peak negative Poisson's ratios) at compressive strains between 0.05 and 0.25. At higher compressive strains, due to the saturation of the rotational degree of freedom of the cells, further rotation will be suppressed. Therefore, inward transverse deformation of the cells will end, and the structure tends to show positive lateral deformations. The positive lateral deformations revert the trends observed in Poisson's ratio-strain curves, pushing the Poisson's ratios to less negative (and eventually positive) values.

The smaller lateral strains and the relatively lower Poisson's ratios in the thick-hinge structures are correlated with the higher internal resistance of the cell hinges against bending, leading to higher overall deformation resistance in the structure. The comparably higher global mechanical strength of the thick-hinge structure (Fig. 6) corresponds well with the deformation and lateral strain measurements discussed earlier. The stress-strain curves obtained under low strain rate compressive loading conditions show an early increase corresponding to the small-strain elastic deformation of the solid hinges, followed by an extended stress plateau. The plateau stress stage is directly correlated with the deformation primarily governed by the rotation of the solid squares. The transition between the stress plateau and the densification phase is marked by hollowed circles in Fig. 6. This transition, *i.e.*, the densification onset, marks the saturation of the rotational degree of freedom of the cells, quantifiable by the maximum energy absorption efficiency metric [15,51,55].

3.4. Deformation and poisson's ratio in intermediate strain rate conditions

Similar analyses were performed on the auxetic structures subjected to intermediate strain rates applied using the drop tower impact instrument. The nominal strain rates in these tests were identified as the slope of the best linear fit to the DIC-measured global strain-time data, as shown in Fig. 7. Accordingly, the resolved strain rates of 204 s^{-1} and 199 s^{-1} were determined for the thin and thick-hinge structures, respectively. The strain rates extracted from Fig. 7 are in excellent agreement with the nominal strain rates calculated based on the drop velocity (*i.e.*, $v = \sqrt{2gh}$) and height of the structures, affirming the dominance of the structural contributions to the overall stress-strain response, as discussed next. The latter conclusion is also consistent with the results of the strain rate sensitivity of the base materials mentioned in Section 3.1. A load cell underneath the samples measured the reaction impact forces, where a 5 mm thick aluminum plate separated the sample and the load cell. Temporal variations of DIC-measured strain and stress (measured directly from the impact loads) recorded for the thin and thick-hinge structures are shown in Figs. 7a and 7b, respectively.

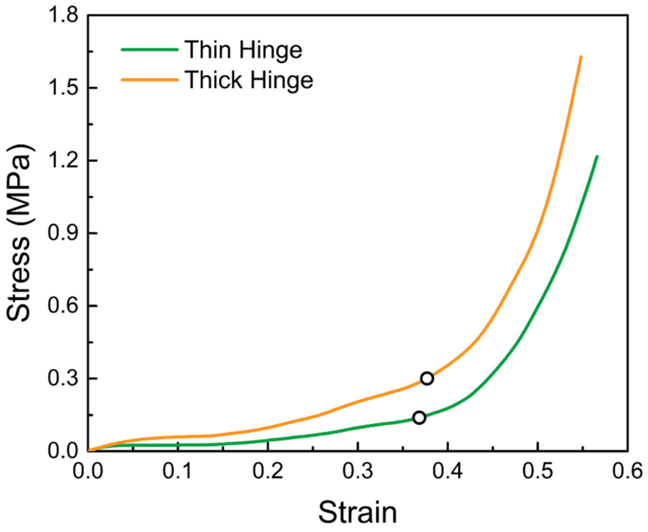

Fig. 6. Engineering stress-strain curves for the thin and thick-hinge structures under a slow strain rate (5×10^{-3} s^{-1}) with hollow circles mark the onset of densification.

The stress-strain responses of the two auxetic structures under an intermediate strain rate were obtained by temporal synchronization of strain and smoothed stress signals, as shown in Fig. 7c. The stress-strain curves reported in this section lack a definitive stress plateau region, possibly due to the strain rate hardening of the structures. Nevertheless, the densification onset strains for each structure were determined by identifying the global strains corresponding with the maximum energy efficiency metrics [51,55,56].

Irrespective of the densification strains and the general shapes of the curves, the two structures show significant strain rate hardening compared with the quasi-static conditions. The increased strain rate also affects the deformation response of the structures. The local deformation response, described earlier by tracking the lateral deformation of cell rows, was also investigated at an intermediate strain rate. Figs. 8a and 8b show the lateral deformation of rows with respect to axial strain for the two structures under impact loading conditions. The two boundary rows (*i.e.*, rows 1 and 6) show lower lateral contractions. However, the difference between the lateral contractions of the boundary rows and middle rows appears less significant compared with low strain rate loading conditions. Nevertheless, the four middle rows show more significant inward deformations, especially in the thin-hinge structure. The spatially-averaged Poisson's ratios for the structures are depicted in Fig. 8d, resembling previous results, except that the Poisson's ratio minima are higher (less negative) at intermediate loading conditions than those observed for slow strain rates. Nevertheless, the two structures retain their highly auxetic nature by showing apparent Poisson's ratios close to -0.8.

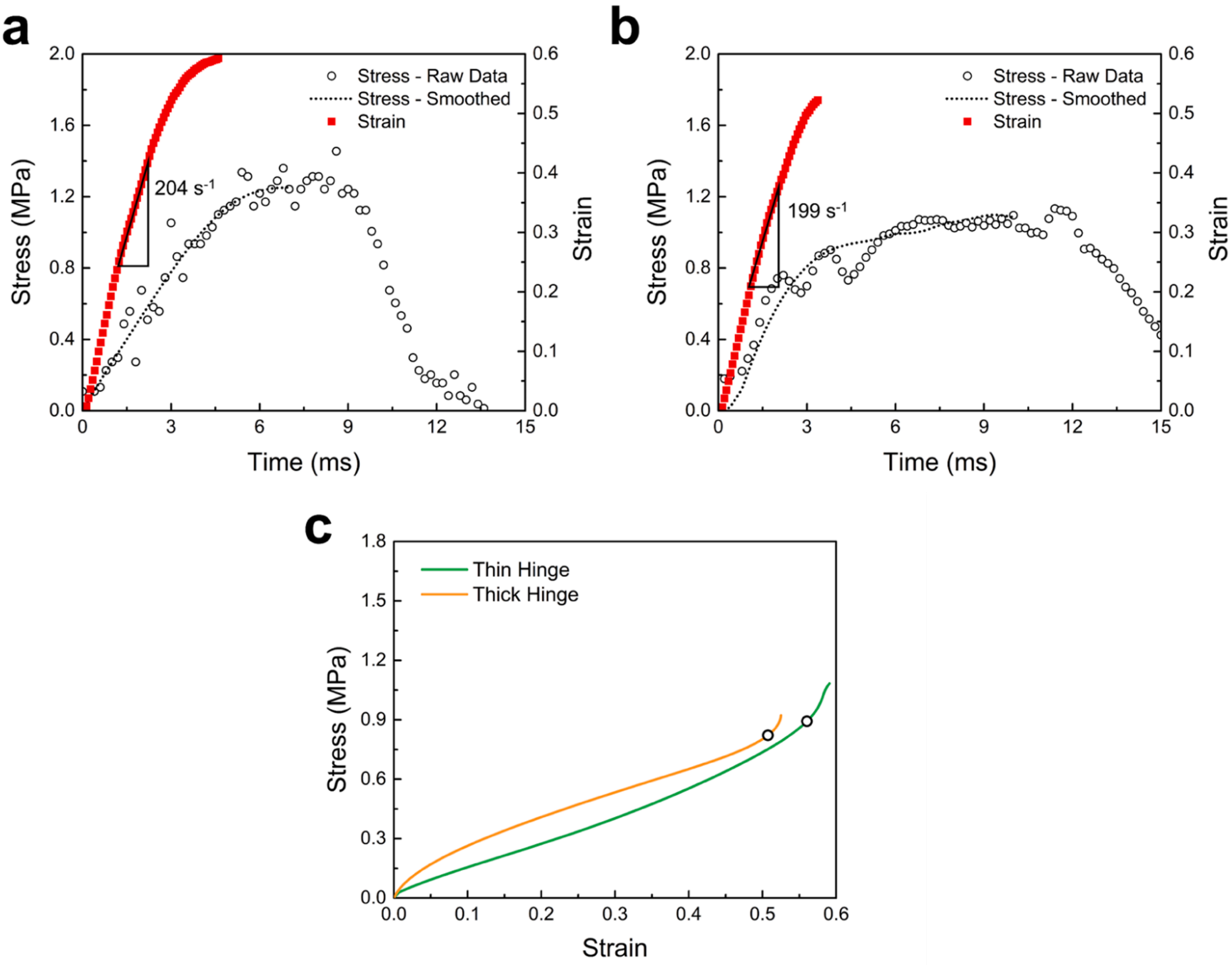

Fig. 7. Temporal stress and strain variations for (a) thin and (b) thick-hinge rotating-squares structures at ~200 s^{-1}. (c) Global stress-strain curves for the two structures (hollow circles denote the onset of densification).

3.5. Deformation and poisson's ratio in high strain rate conditions

The results of deformation analyses for rotating square structures subjected to high strain rate conditions using SHPB are summarized in Fig. 9a, showing the global strain-time histories. Nominal strain rates were resolved by finding the slope of the linear portions of the strain-time curves, *i.e.*, strains > 0.05, as 1973s^{-1} and 1603s^{-1} for the thin and thick-hinge structures, respectively. Figs. 9b and 9c show a sequence of raw images captured at different global strains during high strain rate loading of the two structures. A noticeable difference between the deformation patterns at high, intermediate, and low rates is the distinct row-wise cell rotation and hinge bending heterogeneities, particularly evident in the thin-hinge structure. The cell rows near the top (impact side) of the structure undergo larger rotations and contractions compared with those near the distal (bottom) end. This behavior is particularly evident for the thin-hinge structure.

The heterogeneous deformation patterns can be explained by stress wave propagation and the delayed state of equilibrium in the examined structures. To explain the delayed stress equilibrium, let us assume that at macroscopic scales, the rotating-square structures examined herein behave like solids of equivalent densities and stiffnesses with a theoretical elastic wave speed, C_L [57]

$$C_L = \sqrt{\frac{(1-\upsilon)E}{(1-2\upsilon)(1+\upsilon)\rho}} \tag{4}$$

where, υ, E, and ρ denote macroscale (apparent) Poisson's ratio, elastic modulus, and structure density, respectively. Considering the near-zero initial (elastic) Poisson's ratios identified for the structures in quasi-static conditions (Fig. 5d), Eq. (4) is reduced to $C_L = \sqrt{E/\rho}$. The apparent elastic moduli of the structures were identified from the curves in Fig. 6 as 0.24 and 1.45 MPa for the thin and thick-hinge structures, respectively. The apparent densities were also reported in Section 2.1, enabling the calculation of wave speeds in thin and thick-hinge structures as 21.2 and 49.1 m/s, respectively. Considering the total length of the structures (~17 mm), the corresponding times required for propagation of the elastic sound wave through the sample length are approximately 800 and 337 μs for the thin and thick-hinge structures, respectively, which are longer than the total record time of 256 μs (128 frames at 500,000 fps). On the other hand, as shown in Fig. 9, the 256 μs record time is sufficient to capture large inelastic deformations on the structures, regardless of their hinge thickness. These observations indicate that conventional analysis of deformation response in these structures is challenging, requiring either long test pieces or the application of novel test protocols wherein the non-equilibrium stress conditions can be incorporated through calculation and inclusion of inertia stress fields [58-60]. Nonetheless, visual and DIC strain measurements point to the presence of an 'apparent state of strain equilibrium' at large strains, as discussed in the following. In addition, as shown in the **Supplementary Information** document (**Figure S5**), the forces measured on the impact and distal ends of the sample show significant differences at $t = 0$ to $t =$

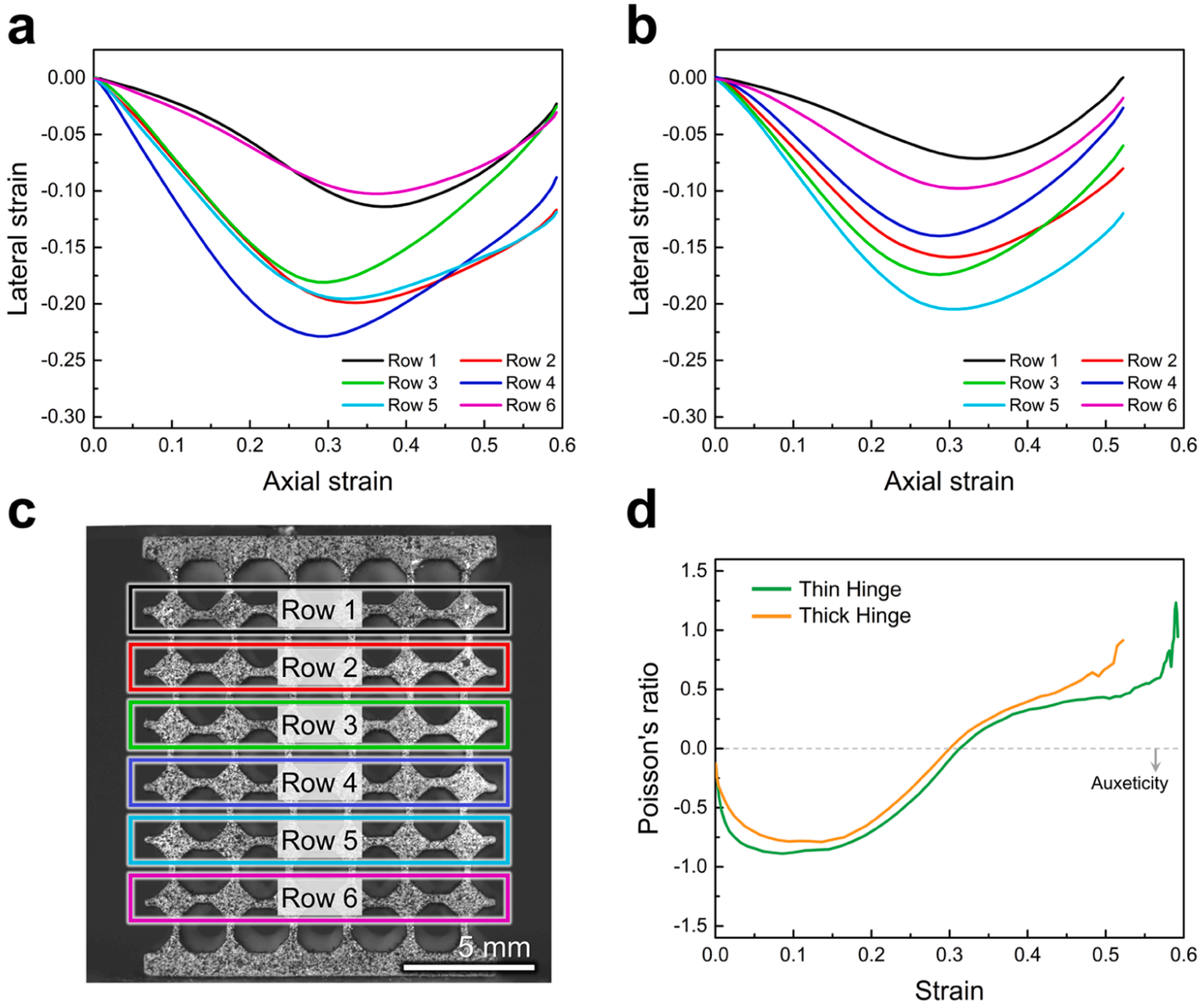

Fig. 8. Evolution of row-wise lateral strains with axial strain for (a) thin and (b) thick-hinge structures under intermediate strain rates ($\sim$200 s^{-1}) as a function of rows, denoted in (c). (d) Respective Poisson's ratio.

200 μs, indicating non-equilibrium conditions. However, the two forces equalize at $t = 200$ μs, exhibiting that equilibrium is established and validating the stresses calculated based on Eq. (2) (*i.e.*, the assuming homogeneous stress and strain distributions). Therefore, the analyses hereafter focus on the timelines after $t = 200$ μs, corresponding to strains greater than 0.2 (see Fig. 9a).

Fig. 10 shows the correlation between lateral and axial strains developed over the six rows (shown earlier in Fig. 8c) under high strain rate loading of the structures. Despite general similarities with previous loading cases (Fig. 5 and Fig. 8), distinct characteristics distinguish the spatial distribution of lateral strains during high-rate loading. First, substantial lags exist between the strains, representing lateral deformation of different rows in the thin-hinge structure (Fig. 10a). This is evident when viewing lateral deformation of axially opposite row numbers (*e.g.*, rows 1 and 6 or 2 and 5). As shown in Fig. 9b, this pattern indicates that delayed deformation onset exists in rows located closer to the distal (bottom) end of the sample. Nonetheless, the four middle rows still show higher inward deformations, confirming the persistence of auxeticity during high strain rate loading.

Secondly, as shown in Fig. 11a, Poisson's ratios for high strain rate conditions show an initially decreasing trend, reaching their respective minima at approximately 0.1 strain. The decreasing trend is inverted for compressive strains > 0.1, reaching near-zero values for compressive strains in the range of 0.22–0.25.

Nominal stress-strain responses of the structures under high strain rate loading are presented in Fig. 11b. Non-equilibrium conditions discussed earlier attributed to underestimated stress values in smaller strain regions due to the simplifying assumptions applied to the SHPB equations in Section 2.4. However, the seemingly homogeneous deformation patterns (Fig. 9) and strain fields (Fig. 10) at global strains >0.25 implicitly indicate the establishment of an apparent equilibrium state, as explained before. Therefore, the stress values within this strain range (*i.e.*, >0.25) were considered for further analyses of strain rate hardening and rate sensitivity, elaborated in the following

3.6. *Strain rate sensitivity of rotating-square structures*

The rate-dependent mechanical behavior of the rotating-square structures was evaluated by quantifying the strain rate dependence of Poisson's ratio and structural strength, as discussed in Section 2.4. For Poisson's ratios, the minimum values measured for each structure at different strain rates were extracted and used for strain rate sensitivity quantifications. The minimum Poisson's ratios were achieved at ~ 0.1 strain, irrespective of the strain rate, making comparative studies reasonable. Fig. 12 shows the variation of Poisson's ratio as a function of the strain rate for rotating squares metamaterials with thin and thick

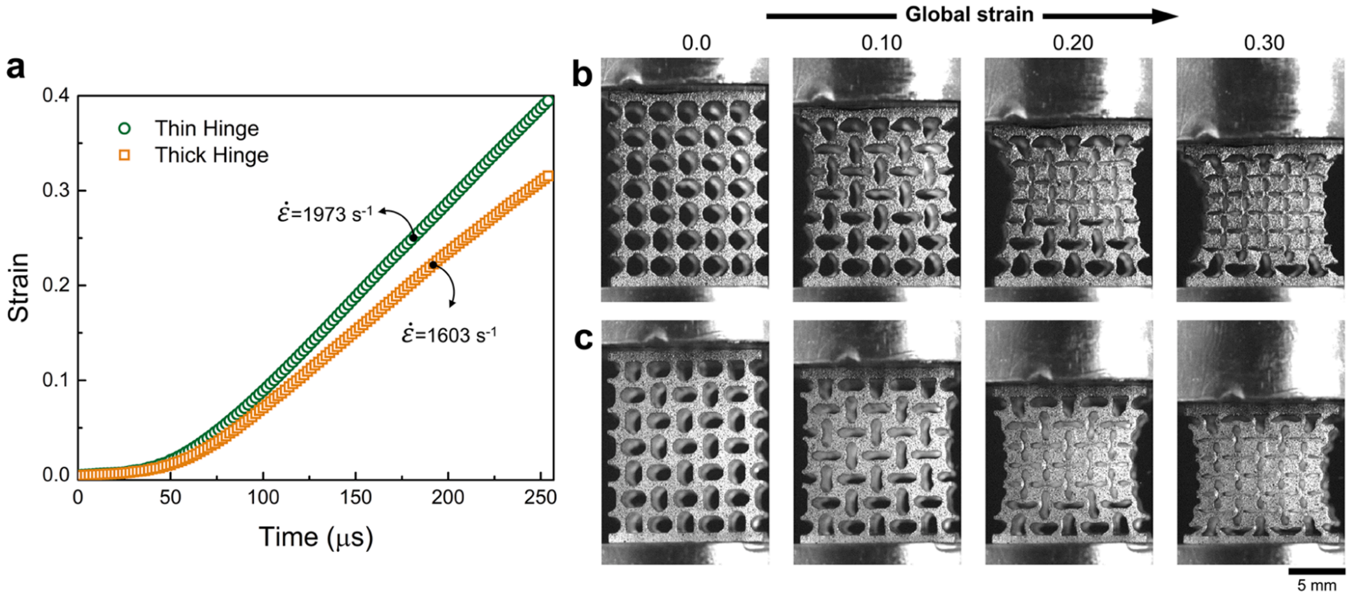

Fig. 9. (a) strain-time histories resolved from ultrahigh-speed imaging, showing the deformation of (b) thin and (c) thick-hinge structures at high strain rate conditions.

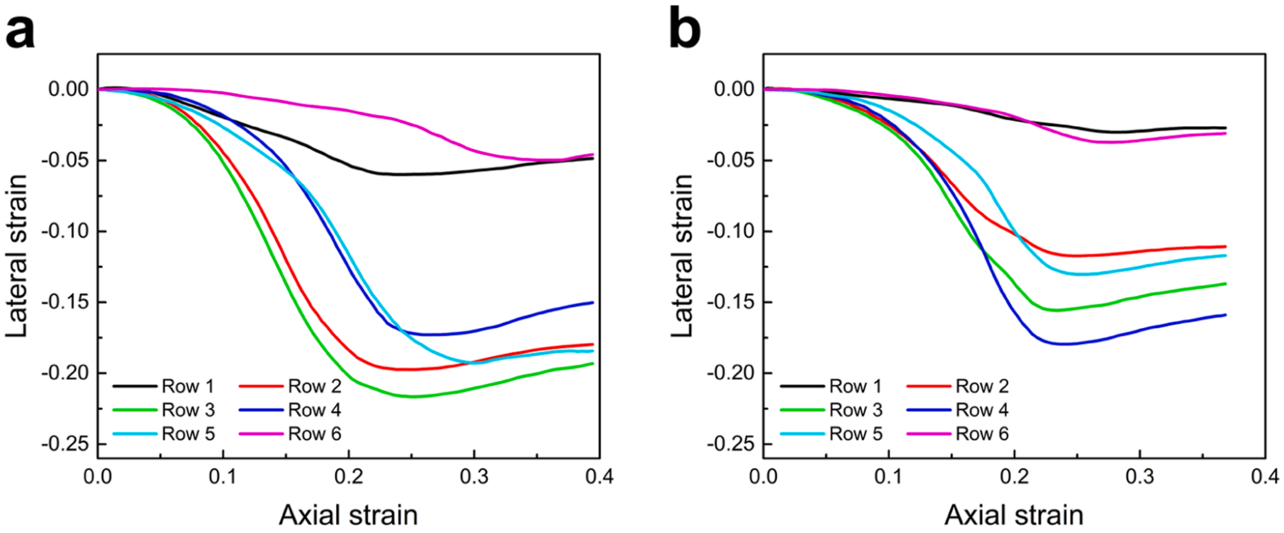

Fig. 10. Evolution of row-wise lateral strains with axial strain for (a) thin and (b) thick-hinge structures at $\dot{\varepsilon}$ >1600s^{-1}.

hinges. A nonlinear correlation between the Poisson's ratio and strain rates is evident for both structures, indicating reduced auxeticity at higher strain rates. This reduced auxetic effect implies higher resistance of the structures against lateral compaction. Similar rate-dependent auxetic behaviors were reported for auxetic polymeric foams [61], Chiral lattices [62], and 2D/3D re-entrant honeycombs made of SS316L alloy [63], with no insight into the possible mechanisms that govern the reduced auxeticity at high strain rates.

The strain rate-induced resistance as a function of lateral deformation stems from three possible interconnected sources. First, as discussed above, increasing stain rate activates complex wave interactions between the axially applied impact load and the wave propagation pattern in the intricate network of solids in the hierarchical structures. Considering the significant contribution of cell hinges to the overall load-bearing response of the structure (see Fig. 4), it is reasonable to assume that thicker cell hinges amplify these wave interaction effects. Second, the higher nominal density of the thick-hinge structure is directly proportional to higher inertia stresses (axial and lateral [64]) developed upon impact, causing higher resistance towards inward transverse deformations.

The third possible source of nonlinearity in Poisson's ratio *vs*. strain rate can be traced to the strain rate hardening of the structures inherited from the base polymer. It was previously shown in polymeric foams under impact [52] that the parent solid (polymer) strain rate sensitivity has significant effects on the strain rate hardening of the derived cellular structures. The highly rate-dependent mechanical response of the parent polymer in this work (see Section 3.1) activates strong rate hardening behaviors in the structures that are combined with the effects of inertia and wave propagation phenomena discussed above. The three intertwined effects increase the resistance to deformation, leading to lower degrees of auxeticity at high strain rates.

Evidence of strain rate hardening behavior in the structures is obtained from the strain rate sensitivity exponent of the structures shown in Fig. 13. In the strain range of 0.25–0.3, a comparison of m_σ values in Figs. 13 and 2b indicates the thin and thick structures show strain rate sensitivity that is substantially higher than the photocurable polymer,

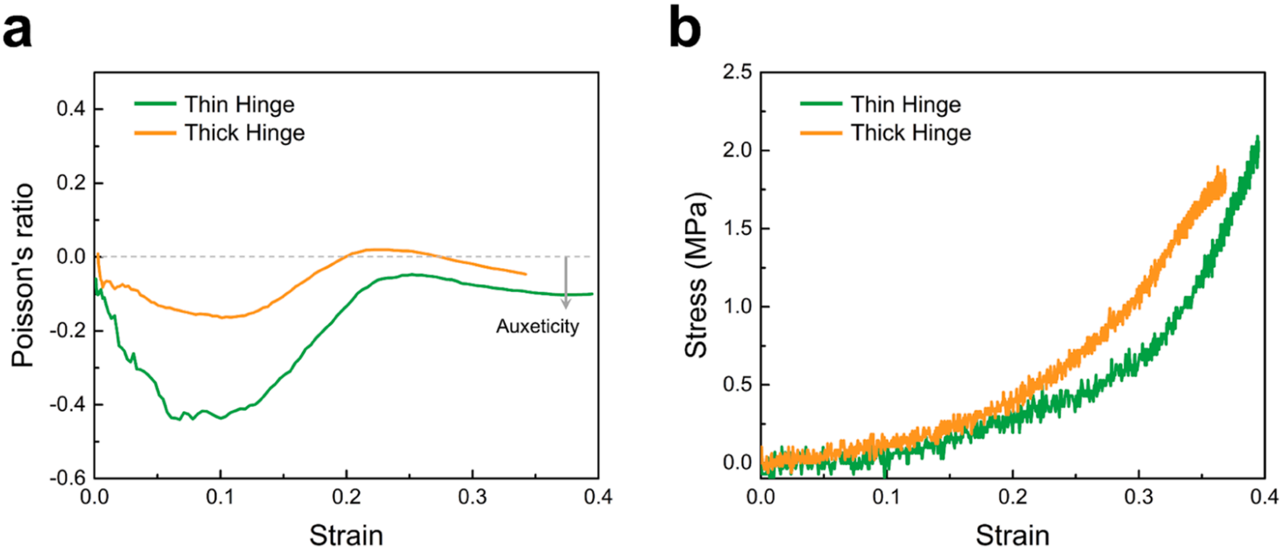

Fig. 11. (a) Variation of Poisson's ratio with axial strain and (b) stress-strain curves for the two structures at high strain rates ($\dot{\varepsilon}$ >1600s^{-1}).

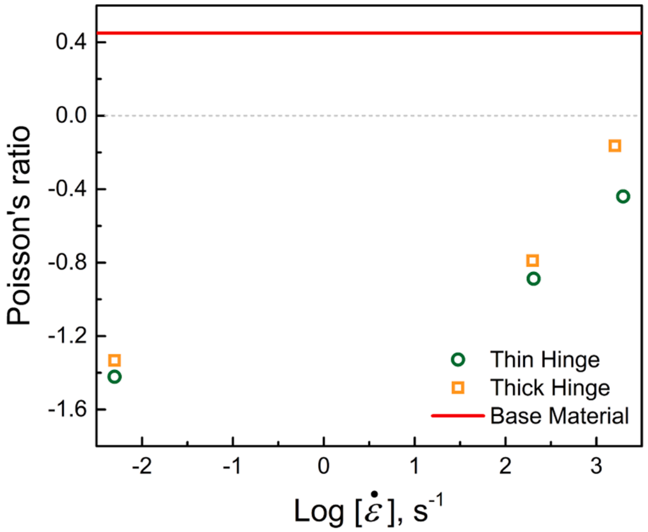

Fig. 12. Poisson's ratio at different strain rates for the thin and thick-hinge structures compared to the base polymer (red horizontal line).

with the thin-hinge structure exhibiting even higher sensitivity. Though the rate sensitivity of the base material and higher inertia effects are directly proportional to the larger solid volume contents in the thick-hinge structure, quantitative data in Fig. 13 indicates a higher degree of apparent rate-hardening for the thin-hinge structure. These observations imply that the stress wave propagation factor contributes to the comparably higher strain rate hardening response. While this conclusion is implicitly realized from the macroscopic measurements carried out in this study, further multiscale investigations are necessary to delineate the competing effects of wave propagation, inertia (at micro and macro scales), and rate-dependent mechanics of the base material in these novel mechanical metamaterials.

4. Conclusions

This study comprehensively investigated the mechanical behavior of additively manufactured rotating-square auxetic polymeric structures subjected to a broad range of strain rates. The experimental approach comprised quasi-static, intermediate, and high strain rate tests that were augmented with high-speed imaging and two-dimensional digital image correlation analyses to obtain specimen deformations. The parent photocurable and flexible 80A resin system exhibited notable strain rate-dependent behavior, directly influencing the mechanical response of the as-manufactured auxetic structures. Multiscale deformation analyses enabled by 2D-DIC carried out under nominally quasi-static deformations revealed a correlation between local and global strains, highlighting the role of cell hinges in the overall deformation and load-bearing characteristics of the structures. Strain fields developed in cell hinges were shown to be proportional to the applied global strains, irrespective of cell hinge thickness, with the evolution of Poisson's ratios under different strain rates highlighting the auxetic nature of the structures. Measurements clearly showed the thick-hinge structures demonstrated lower auxeticity and higher resistance against compressive loads, regardless of the loading rate. Under quasi-static conditions, the Poisson's ratios reached values close to −1.4 in both structures, signifying their strong auxeticity. When subjected to drop tower impact tests (*i.e.*, intermediate strain rate conditions at ~200 s^{-1}), the structures exhibited notable strain rate hardening and lower Poisson's ratios, *i.e.*, lower auxeticity. The strain rate hardening and reduced auxeticity effects were amplified at higher strain rates (>1600s^{-1}) in split Hopkinson pressure bar experiments, with distinct row-wise strain heterogeneities suggesting the delayed onset of deformation in rows near the distal end of the structure.

Results obtained in this study demonstrated the complex interplay between strain rate sensitivity, auxetic behavior, and mechanical strength in rotating-square auxetic structures. The nonlinear relationship between Poisson's ratio and strain rate pointed to a decreased auxetic response at higher strain rates. This phenomenon was attributed to several key factors, including inertia, complex interactions between the elastic and compaction waves in the structures at elevated strain rates, and the inherent strain rate hardening characteristic of the base polymer. Since the apparent strain rate hardening effects were more pronounced in thin-hinge structures, it was inferred that stress wave propagation plays a more significant role in the mechanical response of these structures at high loading rates. Further characterizations of the material *vs.* structural behaviors (including strain rate effects) enabled by finite element simulations are crucial to advance understanding of the strain rate sensitivity of such architected structures.

Supplementary Information

Further information about the baseline tensile tests, impact testing of the base material, imaging systems and DIC parameters, force measurment in SHPB tests, and the photographs of the utilized impact testing

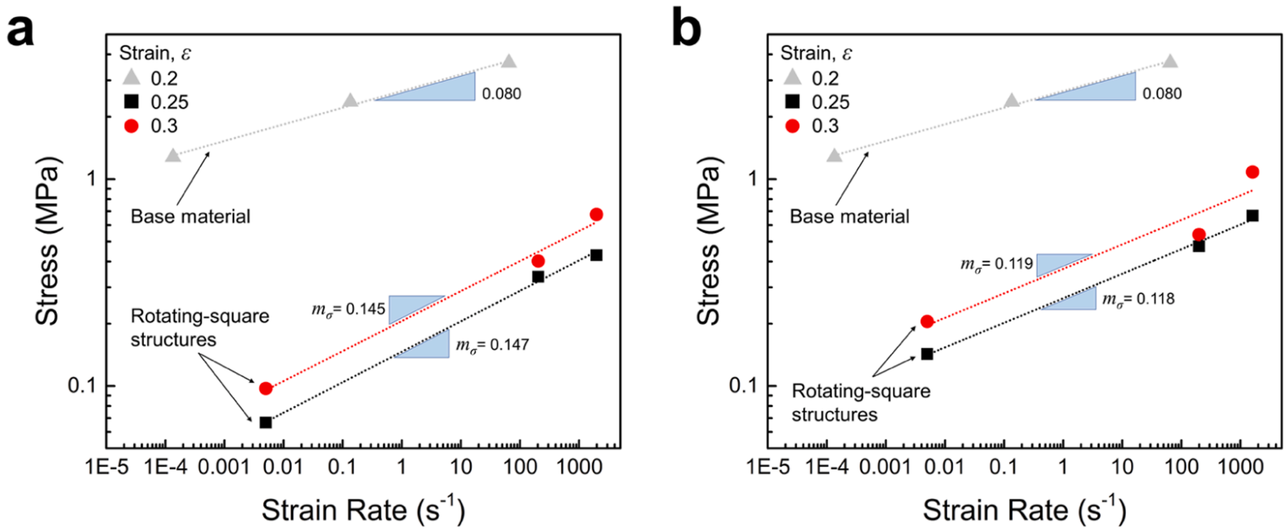

Fig. 13. Stress *vs*. strain rate at different axial compressive strains for (a) thin and (b) thick-hinge structures. Stress-strain rate data for the base material is included for comparison. The slopes of the fitted lines denote the rate sensitivity exponents.

instruments are provided as Supplementary Information.

CRediT authorship contribution statement

Behrad Koohbor: Writing – original draft, Supervision, Funding acquisition, Conceptualization, Validation, Visualization. **Kazi Zahir Uddin:** Writing – original draft, Methodology, Data curation, Investigation. **Matthew Heras:** Writing – original draft, Methodology, Data curation, Investigation. **George Youssef:** Writing – review & editing, Investigation, Conceptualization, Funding acquisition. **Dennis Miller:** Investigation, Resources. **Subramani Sockalingam:** Writing – review & editing, Resources, Investigation. **Michael A. Sutton:** Writing – review & editing, Validation, Resources, Investigation. **Thomas Kiel:** Supervision, Resources, Conceptualization.

Declaration of competing interest

The authors declare that they have no known competing financial interests or personal relationships that could have appeared to influence the work reported in this paper.

Data availability

Data will be available upon request from the corresponding author.

Acknowledgments

This material is based upon work supported by the National Science Foundation under Grant No. 2035660 (B.K.) and Grant No. 2035663 (G. Y.). B.K. gratefully acknowledges the financial support provided by the Advanced Materials & Manufacturing Institute at Rowan University. This work was partially supported by a grant from the Army Research Office W15QKN-21-C-0077. Any opinions, findings, conclusions, or recommendations expressed in this material are those of the authors and do not necessarily reflect the sponsors' views. M.H. gratefully acknowledges the financial support provided by a Wind Institute Fellowship sponsored by the New Jersey Economic Development Authority (NJEDA).

Supplementary materials

Supplementary material associated with this article can be found, in the online version, at doi:10.1016/j.ijimpeng.2024.105128.

References

[1] Bertoldi K, Vitelli V, Christensen J, Van Hecke M. Flexible mechanical metamaterials. Nature Rev Mater 2017;2:1–11.
[2] Surjadi JU, Gao L, Du H, Li X, Xiong X, Fang NX, Lu Y. Mechanical metamaterials and their engineering applications. Adv Eng Mater 2019;21:1800864.
[3] Zhang P, Qi D, Xue R, Liu K, Wu W, Li Y. Mechanical design and energy absorption performances of rational gradient lattice metamaterials. Compos Struct 2021;277: 114606.
[4] Kolken HM, Zadpoor AA. Auxetic mechanical metamaterials. RSC Adv 2017;7: 5111–29.
[5] Lu C, Hsieh M, Huang Z, Zhang C, Lin Y, Shen Q, Chen F, Zhang L. Architectural design and additive manufacturing of mechanical metamaterials: a review. Engineering 2022;17:44–63.
[6] Deng B, Zareei A, Ding X, Weaver JC, Rycroft CH, Bertoldi K. Inverse design of mechanical metamaterials with target nonlinear response via a neural accelerated evolution strategy. Adv Mater 2022;34:2206238.
[7] Ma Y, Feng X, Rogers JA, Huang Y, Zhang Y. Design and application of ‘J-shaped’stress–strain behavior in stretchable electronics: a review. Lab Chip 2017; 17:1689–704.
[8] Pagliocca N, Trkov M, Koohbor B. Modular soft robotic actuators from flexible perforated sheets. Adv Eng Mater 2023.
[9] Zadpoor AA. Mechanical meta-materials. Mater Horiz 2016;3:371–81.
[10] Kadic M, Milton GW, van Hecke M, Wegener M. 3D metamaterials. Nature Rev Phy 2019;1:198–210.
[11] Medina E, Farrell PE, Bertoldi K, Rycroft CH. Navigating the landscape of nonlinear mechanical metamaterials for advanced programmability. Phy Rev B 2020;101: 064101.
[12] Pagliocca N, Uddin KZ, Anni IA, Shen C, Youssef G, Koohbor B. Flexible planar metamaterials with tunable Poisson's ratios. Mater Des 2022;215:110446.
[13] Lakes R. Deformation mechanisms in negative Poisson's ratio materials: structural aspects. J Mater Sci 1991;26:2287–92.
[14] Youssef G, Kokash Y, Uddin KZ, Koohbor B. Density-dependent impact resilience and auxeticity of elastomeric polyurea foams. Adv Eng Mater 2023;25:2200578.
[15] Linforth S, Ngo T, Tran P, Ruan D, Odish R. Investigation of the auxetic oval structure for energy absorption through quasi-static and dynamic experiments. Int J Impact Eng 2021;147:103741.
[16] Uddin KZ, Pagliocca N, Anni IA, Youssef G, Koohbor B. Multiscale strain field characterization in flexible planar auxetic metamaterials with rotating squares. Adv Eng Mater 2023;25:2201248.
[17] Rus D, Tolley MT. Design, fabrication and control of soft robots. Nature 2015;521: 467–75.
[18] Koohbor B, Youssef G, Uddin KZ, Kokash Y. Dynamic behavior and impact tolerance of elastomeric foams subjected to multiple impact conditions. J Dyn Behav Mater 2022;8:359–70.
[19] Farhangdoust S, Aghaei SM, Amirahmadi M, Pala N, Mehrabi A. Auxetic mems sensor. SPIE 2020:118–27. https://doi.org/10.1117/12.2559330.
[20] Lakes R. Foam structures with a negative Poisson's ratio. Science (1979) 1987;235: 1038–40.
[21] Li X, Peng W, Wu W, Xiong J, Lu Y. Auxetic mechanical metamaterials: from soft to stiff. Int J Ext Manufac 2023;5:042003.
[22] Kelkar PU, Kim HS, Cho K-H, Kwak JY, Kang C-Y, Song H-C. Cellular auxetic structures for mechanical metamaterials: a review. Sensors 2020;20:3132.

[23] Chan N, Evans KE. Fabrication methods for auxetic foams. J Mater Sci 1997;32: 5945–53.
[24] Zhai X, Gao J, Liao H, Kirk CD, Balogun YA, Chen WW. Mechanical behaviors of auxetic polyurethane foam at quasi-static, intermediate and high strain rates. Int J Impact Eng 2019;129:112–8.
[25] Kumar N, Khaderi SN, Tirumala Rao K. Elasto-plastic indentation of auxetic and metal foams. J Appl Mech 2020;87:011006.
[26] Yao J, Sun R, Scarpa F, Remillat C, Gao Y, Su Y. Two-dimensional graded metamaterials with auxetic rectangular perforations. Compos Struct 2021;261: 113313.
[27] Grima-Cornish JN, Attard D, Grima JN, Evans KE. Auxetic behavior and other negative thermomechanical properties from rotating rigid units, physica status solidi (RRL)–Rapid research letters, 16; 2022, 2100322.
[28] Mousanezhad D, Haghpanah B, Ghosh R, Hamouda AM, Nayeb-Hashemi H, Vaziri A. Elastic properties of chiral, anti-chiral, and hierarchical honeycombs: a simple energy-based approach. Theoret Appl Mech Letters 2016;6:81–96.
[29] Uddin KZ, Anni IA, Youssef G, Koohbor B. Modulating poisson's ratio in flexible honeycombs by density and architecture gradations. Eng Res Exp 2023;5:045007.
[30] Frenzel T, Kadic M, Wegener M. Three-dimensional mechanical metamaterials with a twist. Science (1979) 2017;358:1072–4.
[31] Rahman O, Uddin KZ, Muthulingam J, Youssef G, Shen C, Koohbor B. Density-graded cellular solids: mechanics, fabrication, and applications. Adv Eng Mater 2022;24:2100646.
[32] Babaee S, Shim J, Weaver JC, Chen ER, Patel N, Bertoldi K. 3D soft metamaterials with negative Poisson's ratio. Adv Mater 2013;25:5044–9.
[33] Lvov VA, Senatov FS, Veveris AA, Skrybykina VA, Díaz Lantada A. Auxetic metamaterials for biomedical devices: current Situation, main challenges, and research trends. Materials (Basel) 2022;15:1439.
[34] Gaspar N, Smith CW, Evans KE. Auxetic behaviour and anisotropic heterogeneity. Acta Mater 2009;57:875–80.
[35] Grima JN, Zammit V, Gatt R, Alderson A, Evans KE. Auxetic behaviour from rotating semi-rigid units, physica status solidi (b), 244; 2007. p. 866–82.
[36] Grima JN, Evans KE. Auxetic behavior from rotating triangles. J Mater Sci 2006;41: 3193–6.
[37] Grima JN, Alderson A, Evans KE. Auxetic behaviour from rotating rigid units, physica status solidi (b), 242; 2005. p. 561–75.
[38] Dudek KK, Gatt R, Mizzi L, Dudek MR, Attard D, Evans KE, Grima JN. On the dynamics and control of mechanical properties of hierarchical rotating rigid unit auxetics. Sci Rep 2017;7:46529.
[39] Gatt R, Mizzi L, Azzopardi JI, Azzopardi KM, Attard D, Casha A, Briffa J, Grima JN. Hierarchical auxetic mechanical metamaterials. Sci Rep 2015;5:8395.
[40] Grima JN, Gatt R, Ellul B, Chetcuti E. Auxetic behaviour in non-crystalline materials having star or triangular shaped perforations. J Non Cryst Solids 2010; 356:1980–7.
[41] Reid DR, Pashine N, Wozniak JM, Jaeger HM, Liu AJ, Nagel SR, de Pablo JJ. Auxetic metamaterials from disordered networks. Proc Nat Acad Sci 2018;115: E1384–90.
[42] Zhang J, Lu G, Wang Z, Ruan D, Alomarah A, Durandet Y. Large deformation of an auxetic structure in tension: experiments and finite element analysis. Compos Struct 2018;184:92–101.
[43] Tang Y, Lin G, Han L, Qiu S, Yang S, Yin J. Design of hierarchically cut hinges for highly stretchable and reconfigurable metamaterials with enhanced strength. Adv Mater 2015;27:7181–90.
[44] Li N, Liu S-z, Wu X-n, Wang J-y, Han Y-s, Zhang X-c. Mechanical characteristics of a novel rotating star-rhombic auxetic structure with multi-plateau stages. Thin-Walled Struc 2023;191:111081.
[45] Sorrentino A, Castagnetti D, Mizzi L, Spaggiari A. Rotating squares auxetic metamaterials with improved strain tolerance. Smart Mater Struc 2021;30:035015.
[46] Slann A, White W, Scarpa F, Boba K, Farrow I. Cellular plates with auxetic rectangular perforations, physica status solidi (b), 252; 2015. p. 1533–9.
[47] Alomarah A, Xu S, Masood SH, Ruan D. Dynamic performance of auxetic structures: experiments and simulation. Smart Mater Struc 2020;29:055031.
[48] Wang J, Luo X, Wang K, Yao S, Peng Y. On impact behaviors of 3D concave structures with negative Poisson's ratio. Compos Struct 2022;298:115999.
[49] Smeets M, Kauvaka P, Uddin K, Koohbor B, Youssef G. Full-field analyses of density-graded elastomeric foams under quasistatic and impact loadings. Adv Eng Mater 2023;25:2300994.
[50] Uddin KZ, Anni IA, Youssef G, Koohbor B. Tuning the mechanical behavior of density-graded elastomeric foam structures via interlayer properties. ACS Omega 2022;7:37189–200.
[51] Uddin K.Z., Heras M., Youssef G., Kiel T., Koohbor B. Multiscale experimental characterization of nonlinear mechanics and auxeticity in mechanical metamaterials with rotating squares.2024. Available at: SSRN https://doi.org/10.2139/ssrn.4864977.
[52] Koohbor B, Ravindran S, Kidane A. Effects of cell-wall instability and local failure on the response of closed-cell polymeric foams subjected to dynamic loading. Mech Mater 2018;116:67–76.
[53] Ravindran S, Tessema A, Kidane A. Multiscale damage evolution in polymer bonded sugar under dynamic loading. Mech Mater 2017;114:97–106.
[54] Hao J, Han D, Zhang XG, Zhang Y, Jiang W, Teng XC, Lang JP, Pan Y, Ni XH, Zhang XY, Xie YM, Ren X. Novel dual-platform lightweight metamaterials with auxeticity. Eng Struct 2022;270:114891.
[55] Li QM, Magkiriadis I, Harrigan JJ. Compressive strain at the onset of densification of cellular solids. J Cell Solids 2006;42:371–92.
[56] Anni IA, Uddin KZ, Pagliocca N, Singh N, Rahman O, Youssef G, Koohbor B. Out-of-plane load-bearing and mechanical energy absorption properties of flexible density-graded TPU honeycombs. Compos Part C: Open Access 2022;8:100284.
[57] Ravindran S, Koohbor B, Malchow P, Kidane A. Experimental characterization of compaction wave propagation in cellular polymers. Int J Solids Struct 2018;139: 270–82.
[58] Koohbor B, Kidane A, Lu W-Y, Sutton MA. Investigation of the dynamic stress–strain response of compressible polymeric foam using a non-parametric analysis. Int J Impact Eng 2016;91:170–82.
[59] Koohbor B, Kidane A, Lu W-Y. Effect of specimen size, compressibility and inertia on the response of rigid polymer foams subjected to high velocity direct impact loading. Int J Impact Eng 2016;98:62–74.
[60] Sockalingam S, Kodagali K, Sutton MA, Miller D, Weerasooriya T. Direct spatio-temporal stress field determination combining full-field deformation measurements and explicit finite element method: concept verification. Ext Mech Lett 2023;65:102106.
[61] Duncan O, Bailly N, Allen T, Petit Y, Wagnac E, Alderson A. Effect of compressive strain rate on auxetic foam. Appl Sci 2021;11:1207.
[62] Mauko A, Fíla T, Falta J, Koudelka P, Rada V, Neuhäuserová M, Zlámal P, Vesenjak M, Jiroušek O, Ren Z. Dynamic deformation behaviour of chiral auxetic lattices at low and high strain-rates. Metals (Basel) 2021;11:52.
[63] Fíla T, Koudelka P, Zlámal P, Falta J, Adorna M, Neuhäuserová M, Luksch J, Jiroušek O. Strain dependency of poisson's ratio of SLS printed auxetic lattices subjected to quasi-static and dynamic compressive loading. Adv Eng Mater 2019; 21:1900204.
[64] Koohbor B, Singh NK, Kidane A. Radial and axial inertia stresses in high strain rate deformation of polymer foams. Int J Mech Sci 2020;181:105679.